Vertical Continuous Compound Casting of Copper Aluminum Bilayer Rods

Thomas Greß[a,*], Vanessa Glück Nardi[b], Simon Schmid[a], Julika Hoyer[a], Yevgen Rizaiev[a], Torben Boll[c,d], Sascha Seils[c,d], Babette Tonn[b], Wolfram Volk[a]

[a] *Chair of Metal Forming and Casting, Technical University of Munich (TUM), Walther-Meißner-Straße 4, 85748 Garching, Germany*
[b] *Institute of Metallurgy, Clausthal University of Technology, Robert-Koch-Straße 42, 38678 Clausthal-Zellerfeld, Germany*
[c] *Institute for Applied Materials (IAM), Karlsruhe Institute of Technology (KIT), Engelbert-Arnold-Straße 4, 76131 Karlsruhe, Germany*
[d] *Karlsruhe Nano Micro Facility (KNMF), Karlsruhe Institute of Technology (KIT), Hermann-von-Helmholtz-Platz 1, 76344 Eggenstein-Leopoldshafen, Germany*

Abstract

A vertical continuous compound casting technology for the production of rotationally symmetric bilayer rods consisting of brass CuZn37 and aluminum AA7075 was developed. The interface of the metallurgically bonded semi-finished products was composed of four intermetallic layers and an anomalous eutectic area of Al_2Cu (θ-AlCu), Al solid solution (α-Al), and other intermetallic precipitates. The intermetallic layers were CuZn (β-CuZn), a suggested two-phase region of $Al_3Cu_5Zn_2$ (τ-AlCuZn) and Cu_5Zn_8 (γ-CuZn), Al_4Cu_3Zn (τ'-AlCuZn), and AlCu (η_2-AlCu). The correlation between the process parameters *casting speed*, *cladding temperature*, and *tool tempering*

*Corresponding author. tel.: +49 89 289 13980; fax.: +49 89 289 13738
Email address: thomas.gress@utg.de (Thomas Greß)
URL: www.utg.de (Thomas Greß)

and the interface formation was studied. The experimental investigations were accompanied by a numerical FEM analysis. The casting speed and the cladding temperature were found to be key factors, that influence the formation of a cohesion between the joining partners.
Keywords: Continuous compound casting, Cohesion, Bimetal, Casting simulation, Interface development, Copper aluminum composite

1. Introduction

Over the past few decades, compound casting has become an innovative and seminal topic with regard to meeting objectives of lightweighting, functional integration, and resource efficiency. The challenge is the combination of disparate metallic materials in a single component to enable a local adaptation of the property profile to the imposed requirements (Stets, 1998). Compound casting is an efficient technology because it offers the potential of integrating the joining operation into the casting process. The mechanisms leading to a metallurgical bonding between the joining partners are complex (Nerl, 2014). According to (Ißleib et al., 1995), the morphology of the interface is influenced by the chemical composition of the base materials, the temperature-time profile during compound casting, the surface roughness and lattice distortion, the operating atmosphere, as well as the hydrodynamic conditions.

Compound casting can be categorized into the joining of similar and dissimilar couples. Similar alloy systems are combinations of Al-Al (Papis et

al., 2008), Fe-Fe (Stets, 1998), and Cu-Cu (Mittler et al., 2019), for example. Dissimilar compound casting is the mix of at least two metals of different alloy systems, such as Al-Cu (Pintore et al., 2020), Al-Mg (Jiang et al., 2018), Al-Fe (Jiang et al., 2015), and Cu-Fe (Dong et al., 2016).

Due to their significantly disparate chemical, mechanical and thermophysical properties, compound casting of copper and aluminum pure metals or alloys is of great academic and industrial importance. Several research studies have focused on casting molten aluminum onto a solid copper insert placed in a steel die or sand mold (Zare et al., 2013). Pintore et al. (2018) investigated the consecutive compound casting of Al-Cu joining couples. After pouring and solidification of pure copper, molten pure aluminum was poured. The aluminum melt wet the solidified substrate body. The static core filling technique was comprehensively analyzed by Luo et al. (2011). Under favorable process conditions, they achieved a bonding between the joining partners, which was based on metallurgical bonding but also on mechanical bonding using solid inserts with different cavity shapes (Luo et al., 2012). The lost foam casting process was also intensively investigated with regard to the compound casting of dissimilar material combinations (Jiang et al., 2016). Along with the studies on compound casting of pure aluminum and pure copper, the usage of aluminum and copper alloys is of particular interest, since the addition of alloying elements enables the extension of the material properties and targeted adaptation to load cases and operating conditions (Fu et al., 2017). Jiang et al. (2019), for instance, examined

the metallurgical joining of pure copper and the A356 aluminum alloy using the lost foam casting technology. The research conducted by Akbarifar and Divandari (2017) and Gholami and Divandari (2018) represents a close relationship to and important basis for the present project. They investigated the static and centrifugal compound casting of the brass/aluminum combination CuZn35/Al.

Continuous compound casting has been a subject of numerous research efforts since the second half of the 20^{th} century. It is highly suitable for the production of cohesively bonded bilayer semi-finished and final products, because it principally features a trade-off between economic and ecological productivity of high-volume metallic products and suitable procedural conditions for the formation of a stable metallurgical bonding. The advantageous process conditions refer to high cooling rates and the overall steady-state thermal profile, which are characteristics of continuous casting technologies (Haga et al., 2009). Remarkable efforts have been made in terms of integrating the joining procedure of aluminum alloys into vertical direct-chill casting operations. Material combinations of AA4045/AA3003 (Xing et al., 2015), AA2024/AA3003 (Zhang et al., 2009), AA6009/AA7050 (Yan et al., 2016), and AA7075/AA6009 (Li et al., 2009) were processed by direct-chill casting. Furthermore, the patented Novelis Fusion$^{\text{TM}}$ process (Anderson et al., 2005) and the research studies by Nerl et al. (2014) and Heugenhauser et al. (2020) on the fabrication of bilayer aluminum slabs and strips have to be mentioned. Vertical (Greß, Mittler et al., 2020) and horizontal (Mittler et

al., 2019) continuous compound casting were comprehensively investigated for the production of bilayer CuSn6/Cu99.5 strips and rods.

Regarding the continuous compound casting of aluminum and copper, the core-filling technology is the main subject of academic analyses. The process is based on the initial casting of a pure copper sleeve using a stationary mold. Subsequently, aluminum is poured into the copper sleeve (Xie et al., 2007). Su et al. (2011) underlined the interdependence between the interface formation and the process parameters, such as pouring temperature, cooling water supply, and casting speed.

Among the past and present industrial and academic studies, the continuous compound casting of brass and aluminum has rarely been scientifically investigated. The formation of metallurgically bonded bilayer components has a significant relevance regarding the fabrication of aquiferous or gas leading pipes in the energy sector or structural components in the medical sector, for example. The present study represents an innovative approach in the development of an industrially-relevant vertical continuous compound casting process for the fabrication of rotationally symmetric rods consisting of brass CuZn37 and the aluminum alloy AA7075. A particular feature is the arrangement of brass as the core material and aluminum as the shell. The present developments are based on the initial investigations on static compound casting and multi-step, semi-continuous compound casting, which were published in (Greß, Glück Nardi et al., 2020). The experimental process analysis is supported by an FEM simulation study, which helped to extract thermal profiles

in the vicinity of the geometrical interface. Procedural key figures enable the technology transfer to other formats of semi-finished products and similar material combinations. Therefore, this study has an extensive importance for the industrial processing of metallic objects.

2. Experimental setup of continuous compound casting

The single-step, continuous compound casting process represents a continuous casting technique, which enables the processing of substrate and cladding material at the same time. The experiments were performed using the continuous casting machine Demag Technica, type 30/10 D I MCP N, from Demag Technica (Veitshöchheim, Germany). The casting machine and the casting tool, which is especially designed for the continuous formation of rotationally symmetric bilayer cast products, are shown in Figure 1. The main components of the casting system were the melt basins, the casting tool, the drawing unit, and the system control from esa4u GmbH (Würzburg, Germany), including the temperature data logging system. The cast materials were melted separately in inductive and resistance-heated furnaces. Commercial brass CuZn37 was applied as the substrate (sub.) and aluminum EN AW-7075 (AA7075) as the shell material. The molten cast materials were poured from the crucibles into the melt basins, which were firmly attached to the casting tool via insulating refractory tool components. The drawing unit consisted of four rolls, which enabled the withdrawal of the solidifying strand in the vertical direction. The casting tool consisted of three

different stages: *substrate casting*, *cladding*, and *compound casting*. The first and third stage were built from graphite molds and copper coolers. The coolers were tempered by individual cooling water circuits. The cladding unit was made from calcium silicate and enabled the aluminum to be fed onto the preformed brass substrate.

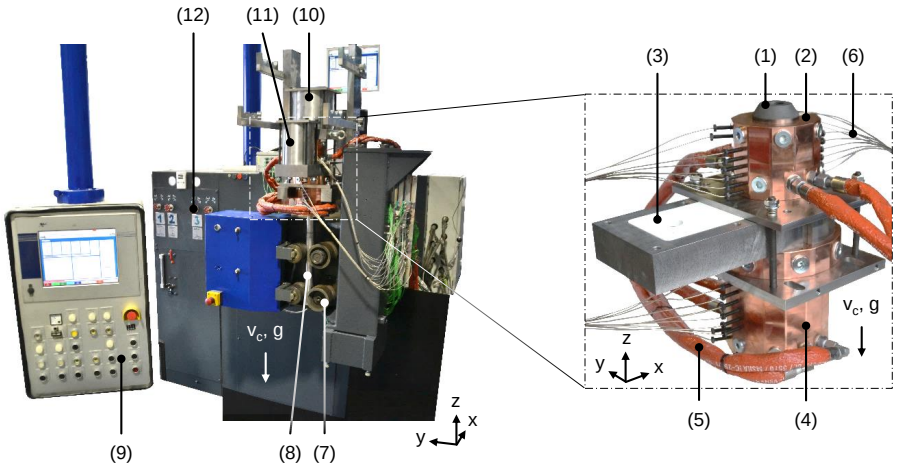

Figure 1: Continuous casting machine and compound casting tool

Figure 2 illustrates the casting tool, the thermocouple measuring positions, and the sample extraction plan. The substrate material was poured into the first casting stage. The solidification of the brass was initiated through the heat transfer from the cast material into the casting tool. The substrate exhibited a nominal diameter of 22.5 mm. The graphite mold of the substrate casting stage was 130 mm long and had an outer diameter of 65 mm. Once the solidified brass substrate entered the cladding unit, it

was wet by molten aluminum AA7075. The cladding unit had a length of 40 mm. The molten shell material flowed into the casting cavity through four equiangularly arranged gates. The drawing unit transferred the bilayer rod to the third casting stage. The latent and thermal energy dissipated into the substrate rod and into the casting tool. The graphite mold of the compound casting stage was 200 mm long and had an inner diameter of 45 mm and an outer diameter of 100 mm. The graphite molds were manufactured from G330 graphite from TOKAI CARBON DEUTSCHLAND GmbH (Buchholz-Mendt, Germany), and the copper coolers from AMPCOLOY®972 from AMPCO METAL Deutschland GmbH (Geretsried, Germany). Thermocouples (type K, class 1, diameter 1.5 mm) were utilized to record the thermal profile during compound casting with a frequency of 1 Hz. 23 thermocouples T_{Mold} were located in the graphite molds at different z-positions at a distance of 3 mm from the casting cavity. The copper coolers were equipped with 19 thermocouples T_{Cooler} at different z-positions at a distance of 3 mm from the inner surface. Additionally, the pouring temperature of the cast materials was measured in the melt basins.

The interdependence between the process conditions and the interface formation was assessed by optical and mechanical characterization methods. Samples were extracted from as-cast bilayer rods. One sample batch consisted of a cross-sectional structural, a longitudinal structural and three push-out specimens. The latter ones had a thickness of 2 mm. The samples were taken from the cast product section, which was formed under quasi-

stationary thermal conditions. The beginning of the stationary state strongly depends on the experimental configuration applied. It was assumed that the steady state begins at a minimum strand length of 300 mm.

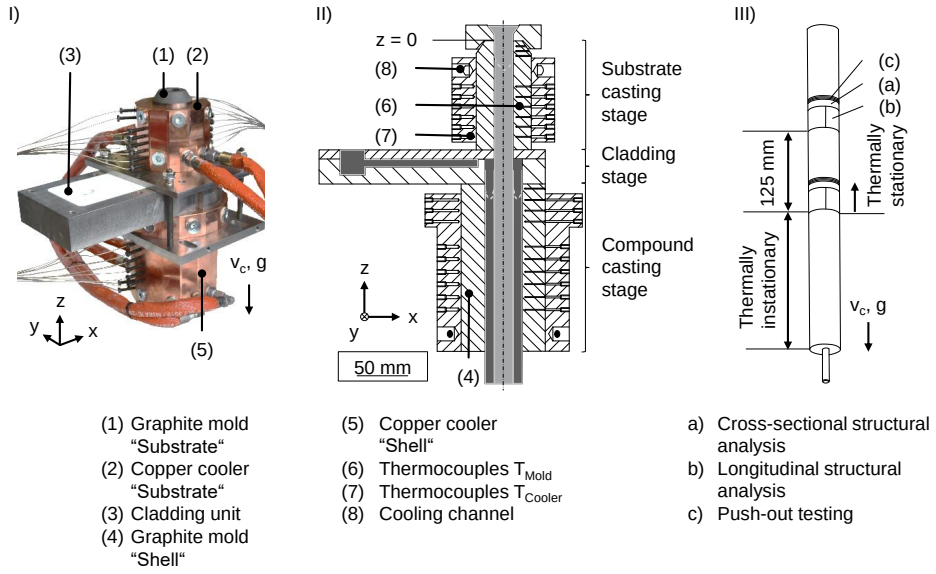

Figure 2: I) Continuous compound casting tool, II) schematic diagram of the thermocouple measuring positions and III) sample extraction plan

The compound casting process was initiated by drawing a steel dummy bar out of the casting tool in the vertical direction. Thus, the substrate and shell cavity opened simultaneously. An intermittent drawing kinematics was applied. Different strand drawing strategies are provided in Figure 3. The friction between the rim zone of the solidifying strand and the casting tool is a significant disadvantage of continuous casting with stationary molds. It can cause surface damages or even a strand tear-off. The continuous drawing strategy is primarily applied for casting systems with movable mold walls, whereas cyclical go-stop withdrawals were developed especially for stationary

mold systems. One cycle consists of a stroke, a waiting time, and eventually a back-stroke. The waiting time promotes the formation of a stable rim zone to overcome the friction forces caused by the relative motion between the strand and the mold wall. The nominal casting speed v_c is the arithmetic mean value of the actual casting speed v over the process time t. To guarantee rapid heating of the tool components and avoid a premature solidification of the cast materials, an initial starting stroke with a length of 50 mm was applied. Subsequently, go-stop kinematics with a cyclical repetition of stroke, executed as a triangle function of casting speed v and stroke time t_s, and a waiting time t_w were chosen.

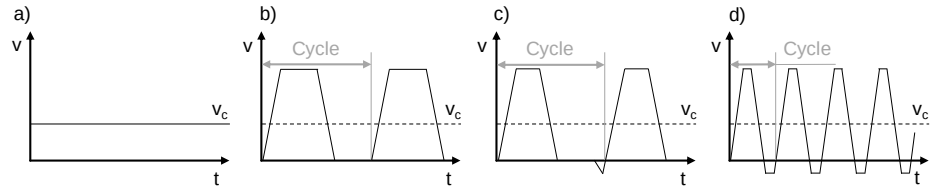

Figure 3: Kinematics of strand withdrawal: a) continuous, b) go-stop, c) go-stop-back, and d) high cyclical according to (Nerl, 2014) and (Ricken, 2008)

The process window of continuous compound casting was experimentally and numerically evaluated by varying different process parameters. The key parameters to span the test field were the average casting speed v_c, the tool cooling conditions, and the temperature of the cladding material. The detailed procedural configurations are presented in the respective paragraphs. The casting speed was expected to provide the greatest influence on the interface formation, as the thermal profile of both the substrate and the

cladding is directly affected by the enthalpy input into the casting system. However, an increase in the casting speed often lowers the process stability. This can be countered by e.g. raising the flow rate of the cooling water. It can be concluded that the continuous compound casting process is highly complex. Different key parameters have to be taken into consideration to find the optimum regarding process stability and interface formation. These are not strictly coupled. However, the resulting effects of a single parameter can be reinforced or compensated by other parameters.

3. Numerical setup

The experimental process investigations were accompanied by a finite element method (FEM) study. The simulations were performed using the commercial software tool WinCast® from RWP GmbH (Roetgen, Germany). The simulation algorithm is based on the coupling of the Fourier's heat transfer equation with the Navier-Stokes equations, and the law of the conservation of mass and momentum (Nerl et al., 2014). To reduce the computational effort, the FEM model was built up as a quarter of the actual casting system (see Figure 4) exploiting the largely rotational symmetry. The node distance of the meshed model was 1.9 mm in the z-direction. The substrate and the shell melt supplies were modeled as components with a constant temperature over the simulation time. The cooling water flow was approximated by model parts with a constant temperature, which amounted to the mean value of the experimental inlet and outlet temperature. The strand withdrawal was sim-

ulated by the imposition of a temperature field shift according to the average casting speed and a coupled fluid flow calculation. This means that a constant casting speed condition and additionally a fluid flow simulation of the liquid cast material fraction was defined to model the material flow.

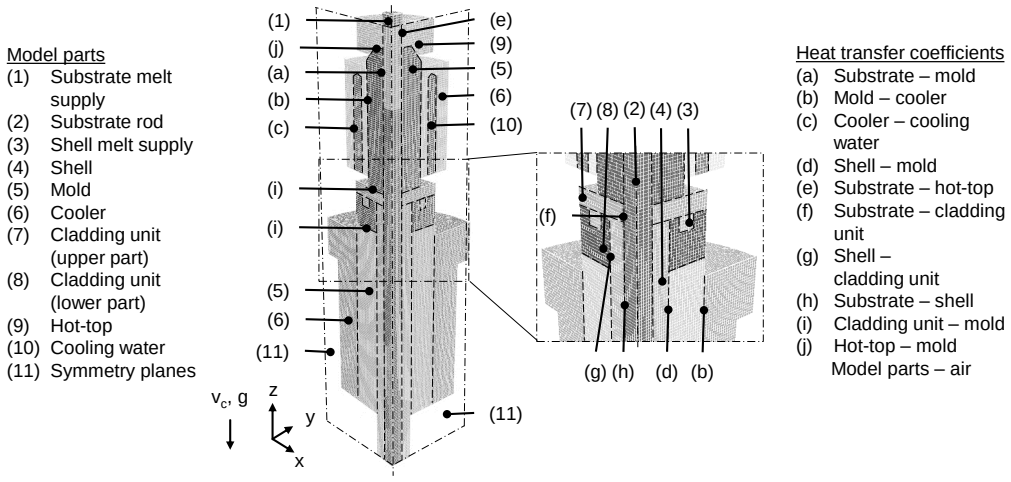

Figure 4: Simulation setup of vertical continuous compound casting

The heat transfer coefficient (HTC) between system components is of particular importance with regard to achieving a calibrated and validated simulation model. The HTCs between the cooling water and the copper coolers were calculated according to (Gnielinski, 1976). Important boundary conditions and HTCs of the simulation model are presented in Table 1. Regarding the cast alloys and the respective tool components, the given HTC range spans the solidification interval of the cast material. The lower limit refers to the solidus point, whereas the upper limit refers to the liquidus point. The HTC between the cast alloys and the graphite molds were cal-

culated in accordance with previous investigations on continuous compound casting of bilayer aluminum strips conducted by Nerl et al. (2014). The heat transfer between the graphite mold and the copper cooler depends on the contact conditions between the components, which are subjected to physical and mechanical properties, the contact pressure, as well as the surface roughness. The heat transfer between the substrate and the shell is of major importance. The heat exchange is primarily conductive. Nerl et al. (2014) and Heugenhauser et al. (2020) assumed that the heat transfer between joining partners with the same base material (e.g. AlSn6Cu-Al99.5) is nearly ideal with approximately $1 \cdot 10^6\ W\ m^{-2}K^{-1}$. The assumption includes a good wetting between the substrate and the cladding, as well as the absence of interfacial oxide layers and intermetallic phases, which inhibit the heat flow. The thermal conductivity of zinc-based intermetallic phases at the interface of an Al-Cu joint couple was investigated by Klose et al. (2018). Due to the significantly lower thermal conductivity of intermetallic layers in contrast to most of the aluminum and copper alloys, the HTC was determined to be $50,000\ W\ m^{-2}K^{-1}$ at temperatures below the solidus point of the lower melting cast alloy.

Property	Value
HTC between CuZn37 and AA7075	$50,000 - 990,000\ W\ m^{-2}K^{-1}$
HTC between CuZn37 and graphite mold	$800 - 80,000\ W\ m^{-2}K^{-1}$
HTC between AA7075 and graphite mold	$4,000 - 80,000\ W\ m^{-2}K^{-1}$
HTC between graphite mold and copper cooler (substrate casting stage)	$50,000\ W\ m^{-2}K^{-1}$
HTC between graphite mold and copper cooler (compound casting stage)	$7,000\ W\ m^{-2}K^{-1}$
HTC between casting tool components	$100 - 5,000\ W\ m^{-2}K^{-1}$
Substrate melt temperature (constant)	960 °C
Shell melt temperature (constant)	750 °C, 850 °C
Initial graphite mold temperature	60 °C
Initial copper cooler temperature	60 °C
Temperature of surrounding air (constant)	21 °C

Table 1: Boundary conditions and heat transfer coefficients (HTC) between simulation components

Figure 5 shows an exemplary temperature field simulation of single-step, continuous compound casting. The process starts at the time $t = 0\ s$. Due to the enthalpy input of the cast materials, a temperature rise is apparent in the casting system. The steady state is achieved no later than at 100 s. The interfacial temperature profile is extracted for the thermally stationary state. The solidification of the substrate is initiated at the transition between insulating hot-top and graphite mold. The solid substrate rod is wet by the shell material at a z-position of -140 mm. The further curve progression displays the solidification of the aluminum layer and the cooling phase of the compound rod. As quasi-stationary conditions are key characteristics of continuous casting processes, the steady state results are used for the

following procedural investigations and discussions.

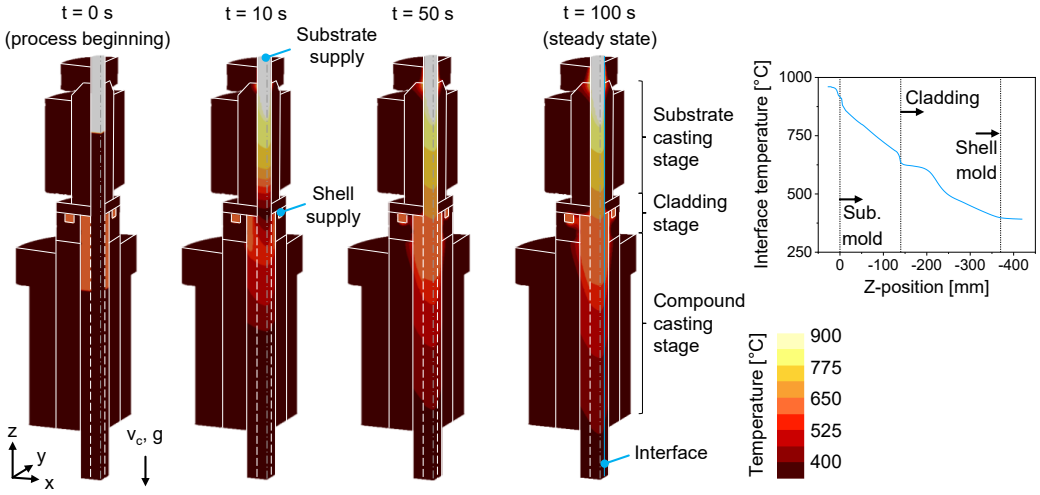

Figure 5: Simulated temperature field of vertical continuous compound casting of CuZn37/AA7075 bilayer rods

The above shown HTCs were determined in an iterative calibration process through the comparison between the experimental and numerical results, as demonstrated by Nerl et al. (2014). The comparison between experiment and simulation is illustrated in Figure 6 for three different casting speeds. A high accuracy of the numerical model is achieved, as the simulated thermal profiles of the casting tool match well with the experimentally determined ones. The calibrated and validated simulation model enabled the extraction of procedural key figures. Consequently, the simulation model represents a digital twin of the experimental casting process and decisively supports the evaluation of the influence of process parameters on the interface formation.

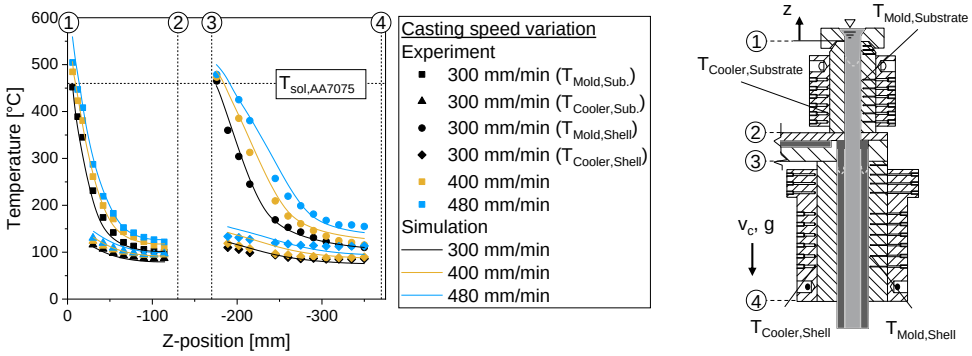

Figure 6: Calibration of the simulation model of continuous compound casting

4. Materials and characterization methods

The applied cast materials were brass CuZn37 (62.27 m-% Cu and 37.70 m-% Zn) and aluminum AA7075 (90.05 m-% Al, 5.48 m-% Zn, 2.20 m-% Mg, and 1.63 m-% Cu). Brass in the amount of approximately 4.5 kg was poured into the casting system at a temperature of about 1050 °C, as was aluminum in the amount of 4.5 kg at a temperature of 800 °C and 900 °C, respectively. The thermophysical properties of CuZn37 and AA7075 were examined using differential scanning calorimetry (DSC), laser flash analysis (LFA), dilatometry, and thermogravimetric analysis. Details on the testing methods and results are published in (Greß, Mittler et al., 2019) and (Greß, Glück Nardi et al., 2020). A concise summary of important thermophysical data is presented in Table 2.

Property	CuZn37	AA7075
Solidus temperature T_{sol}	899 °C	466 °C
Liquidus temperature T_{liq}	925 °C	640 °C
Specific latent enthalpy	139 $J\ g^{-1}$	348 $J\ g^{-1}$
Specific heat capacity at T_{sol}	0.47 $J\ g^{-1}K^{-1}$	1.08 $J\ g^{-1}K^{-1}$
Specific heat capacity at T_{liq}	0.48 $J\ g^{-1}K^{-1}$	1.13 $J\ g^{-1}K^{-1}$
Thermal conductivity at T_{sol}	121 $W\ m^{-1}K^{-1}$	151 $W\ m^{-1}K^{-1}$
Thermal conductivity at T_{liq}	68 $W\ m^{-1}K^{-1}$	69 $W\ m^{-1}K^{-1}$

Table 2: Thermophysical data of CuZn37 and AA7075 according to (Greß, Mittler et al., 2019) and (Greß, Glück Nardi et al., 2020)

The structural analysis of as-cast bilayer samples was performed using light optical microscopy (LOM) and scanning electron microscopy (SEM). The ZEISS Axioplan 2 LOM device from Carl Zeiss Microscopy GmbH (Jena, Germany) and the TM3030 Plus SEM instrument from Hitachi High-Technologies Corp. (Tokyo, Japan) were utilized. The LOM analysis was conducted using etched and unetched samples. The applied etching agent was a combined preparation of a two-step color etching according to Weck and Leistner and a Klemm II etching. Additionally, energy-dispersive X-ray spectroscopic analyses (EDS) were conducted in order to determine the chemical composition and phase fraction of the near-interface area. The respective analytical devices were equipped with the SphinX 133 EDS unit from eumeX Instrumentebau GmbH (Heidenrod, Germany) and the Oxford 40 Ultim® Max EDS unit from Oxford Instruments Ltd. (Abingdon, United Kingdom). The crystallographic orientation of intermetallic layers was examined by electron backscatter diffraction (EBSD). The EBSD device used was

the Oxford Symmetry® instrument from Oxford Instruments Ltd. (Abingdon, United Kingdom). The EDS mapping and the EBSD were carried out by the Institute of Materials Science and Mechanics of Materials (Munich, Germany).

The phase fraction analysis was supported by atom probe tomography (APT) measurements, which were performed at the Karlsruhe Nano Micro Facility (Eggenstein-Leopoldshafen, Germany) with the LEAP 4000X HR device from CAMECA SAS (Gennevilliers Cedex, France). The APT tips were extracted by focused ion beam (FIB) methods using the Zeiss Auriga® 60 FIB-SEM device from Carl Zeiss Microscopy GmbH (Jena, Germany). The APT laser measuring technique was applied. The laser measurement was taken with a pulse rate of 125 kHz at a sample stage temperature of 50 K. APT was used to analyze the phase composition and element distribution at a nanoscale. The examination was accompanied by statistical methods, such as the frequency distribution analysis. This technique mathematically calculates the probability distribution of randomly chosen and actually distributed elements within an area (Moody et al., 2008).

The interfacial bonding strength was examined by push-out testing. It is a commonly applied quasi-static characterization method for rotationally symmetric bilayer compounds and comprehensively experimentally and numerically investigated as shown in (Greß, Stahl et al., 2019) for CuSn6/Cu99.5 and AA7075/AA6060 hybrids, as well as in (Greß, Gruber et al., 2020) for CuZn37/AA7075 bimetals. The push-out tool was attached to the Z150

universal testing machine from Zwick Roell AG (Ulm, Germany). The disk-shaped sample was placed and centered on the die (lower active element). The punch (upper active element) moved downward with a constant speed of 1 mm min^{-1}. The compression load induced shear stresses in the bilayer sample, which finally led to the failure of the hybrid structure. The bonding strength was calculated as the ratio of maximum compressive testing force and interface area. The nominal interface diameter was 22.5 mm. The ratio of punch diameter and inner die diameter was 21.5/24.0 mm.

5. Results and discussion

5.1. Interface formation and character

The metallurgical bonding between the dissimilar joint couple Al-Cu is characterized by a distinct chemical reaction between the base materials. Whereas the compound casting of pure aluminum and pure copper has widely been scientifically investigated, there is hardly any research focusing on alloyed Al-Cu systems. Due to complex dissolution, precipitation and diffusion processes at the interface of alloyed Al-Cu compounds, an uncertainty still exists regarding the formation and type of intermetallic phases. The interfacial area of brass/aluminum compounds exhibits four different regions at a macroscopic scale: firstly, the brass base material, secondly, the aluminum alloy base material, thirdly, an anomalous eutectic area, and, lastly, various layered intermetallic phases, so-called *intermetallic layers (IMLs)*. Figure 7 illustrates exemplary micrographs of the near interface region of

as-cast CuZn37/AA7075 compounds.

The research conducted by Akbarifar and Divandari (2017) and Gholami and Divandari (2017) are of particular importance for the present study, as the scientists conducted experiments on the compound casting of brass and aluminum. They designated the area between the aluminum base material and the IMLs as anomalous eutectic, which is composed of aluminum solid solution (α-Al) and Al_2Cu (θ-AlCu) and other intermetallic precipitates. The anomalous eutectic is a result of undercooling processes of the aluminum melt close to the brass surface. The Al-Cu eutectic solidifies under formation of irregular Al_2Cu precipitates or undulated eutectic microstructures with Al solid solution and Al_2Cu lamellae (Bogno et al., 2019). It was stated that the irregular eutectic is formed under conditions of internal heat flow during the initial solidification (Mueller and Perepezko, 1988). The space between the θ-AlCu phases is characterized by a significant degree of porosity. The formation of porosity in Al-Cu compounds has been discussed by Prasad et al. (2004). The coarse microstructure of θ-AlCu phases inhibits the melt flow, which leads to unfavorable feeding conditions.

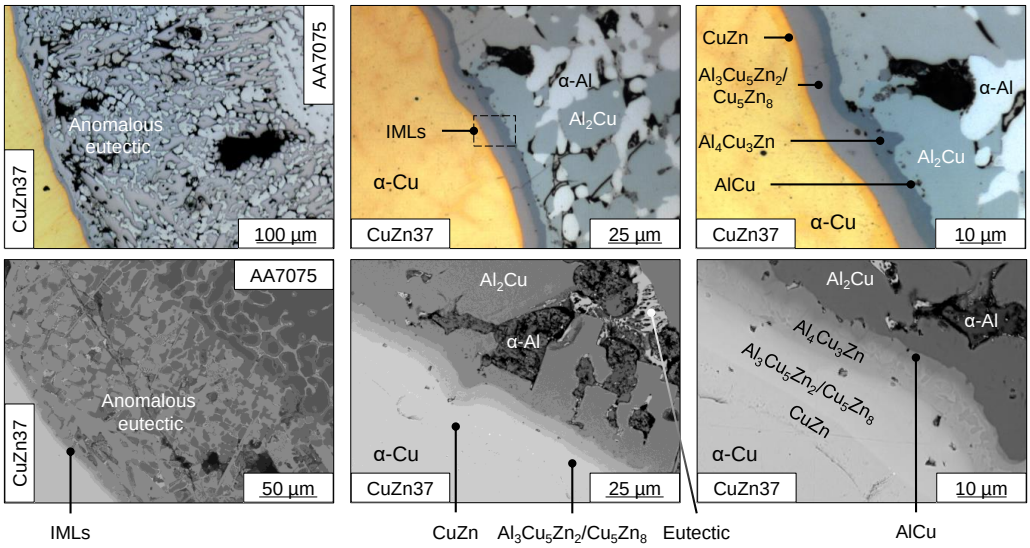

Figure 7: LOM and SEM analyses of the interfacial structure of as-cast CuZn37/AA7075 compounds

The chemical composition and type of the IMLs were determined using EDS analysis and thermodynamic simulations. The identification of various IMLs in the ternary Al-Cu-Zn system is comprehensively discussed in (Greß, Glück Nardi et al., 2020). Figure 8 shows a representative EDS line scan of as-cast brass/aluminum compounds, as well as the isothermal section at 400 °C and the projected diffusion path of an experimental EDS line scan. Four discernible IMLs were identified. In accordance with the literature, they were determined to be CuZn (β-CuZn), $Al_3Cu_5Zn_2$ (τ-AlCuZn), Al_4Cu_3Zn (τ′-AlCuZn), and AlCu (η_2-AlCu). Several intermetallic phases of the ternary Al-Cu-Zn system and the chemical reaction leading to those compositions are still unexplored. As can be seen in the isothermal section in Figure 8, the diffusion path passes through the two-phase region of τ-AlCuZn and Cu_5Zn_8

(γ-CuZn). However, a clearly discernible two-phase character cannot be derived from the EDS line scan analysis. Therefore, the phase character of the suspected two-phase region was reviewed by EDS mapping, EBSD, and APT techniques.

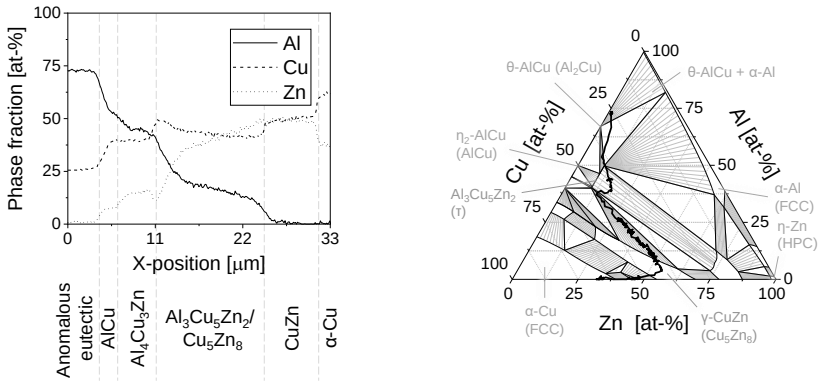

Figure 8: EDS line scan across the interface of as-cast brass/aluminum bilayer samples and diffusion path projection onto isothermal section according to (Greß, Glück Nardi et al., 2020)

Figure 9 shows the results of the EDS mapping and EBSD of the suspected τ-AlCuZn/γ-CuZn layer. Both the γ-CuZn and τ-AlCuZn phase exhibit a cubic crystal structure. Whereas γ-CuZn is characterized by a space group of $I\bar{4}3m$ (Degtyareva et al., 2005), τ-AlCuZn has a space group of Pm3m (Eckerlin et Kandler, 1971). The chemical reference compositions for the colored EDS phase mapping were 38 at-% Cu and 62 at-% Zn for γ-CuZn, as well as 16 at-% Al, 64 at-% Cu, and 21 at-% Zn for τ-AlCuZn. The results revealed a polycrystalline character of the IML. The chemical composition of the grains is inhomogeneous. Single grains with a pronounced τ-AlCuZn composition can be found, whereas most grains exhibit a blending

of τ-AlCuZn and γ-CuZn. A demarcated coexistence of both phases was not identified. The phase character rather resembles a mixed composition with a spatial inhomogeneity similar to segregation phenomena.

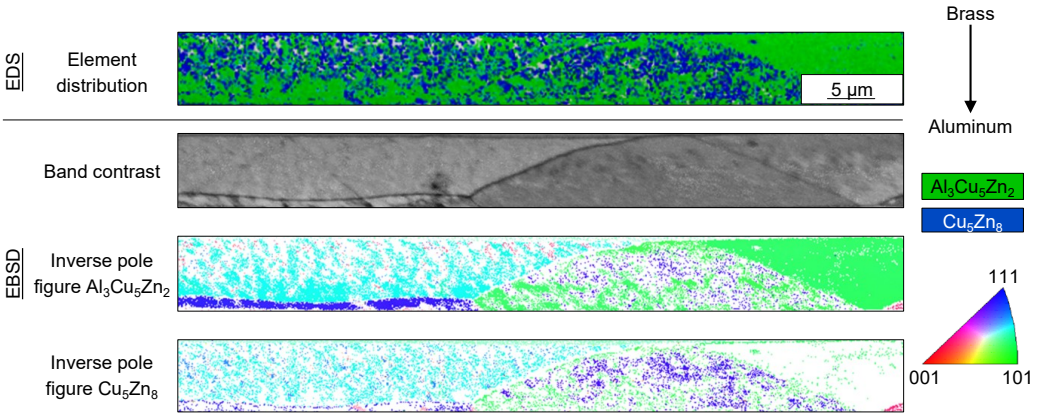

Figure 9: EDS mapping and EBSD analysis of the suspected two-phase region

The sample analyzed by APT was extracted from the center of the suspected two-phase region. The in-plane concentration profile and the frequency distribution analysis are shown in Figure 10. The frequency distribution analysis provides a comparison between the binomial distribution of chemical elements and the experimentally determined distribution. The APT measurement yielded an overall composition of 45 at-% Cu, 40 at-% Zn, and 15 at-% Al. This largely correlates with the EDS line scan result. The in-plane concentration profile pointed out variations in the element concentration. A distinct interface between two suspected phase was not observed. However, the inhomogeneity in the element distribution at the nano-scale was documented. The frequency distribution analysis mathematically calcu-

lates the inhomogeneous element distribution with μ-values of 0.83 for Al, 0.45 for Cu, and 0.92 for Zn. The results suggest that the investigated area constitutes a single phase of τ-AlCuZn with Zn-rich clusters. These clusters are characterized by a Zn concentration of about 70 at-%.

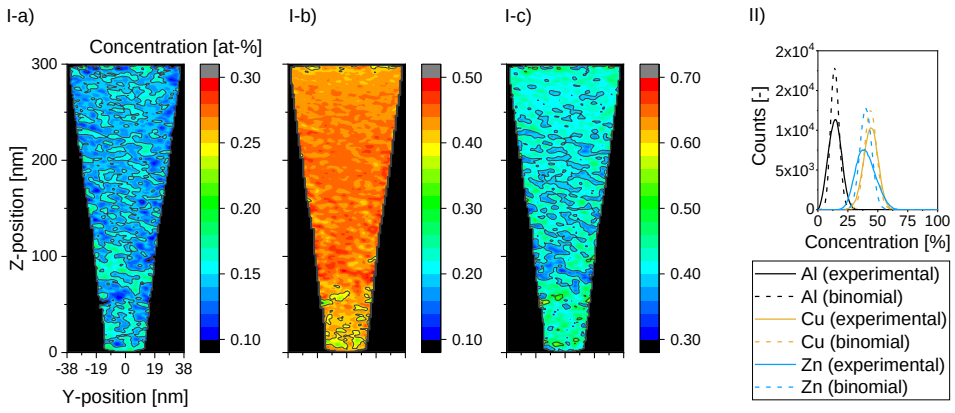

Figure 10: Atom probe tomography of the $Al_3Cu_5Zn_2/Cu_5Zn_8$ IML: I) in-plane concentration profile (a) Al, b) Cu, and c) Zn) and II) frequency distribution analysis

The formation of the anomalous eutectic area is caused by the dissolution of copper and zinc in the aluminum melt. The process is schematically illustrated in Figure 11. Due to the dissolution, the interface geometrically deforms and τ-AlCuZn phases are formed at the substrate surface. Subsequently, θ-AlCu phases grow, detach, and distribute in the aluminum melt. (Divandari and Vahid Golpayegani, 2009)

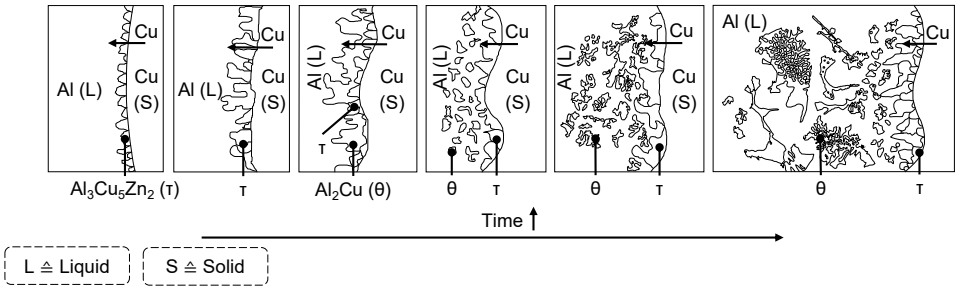

Figure 11: Diagram of copper dissolution in molten aluminum alloy according to (Divandari and Vahid Golpayegani, 2009)

The formation of IMLs is primarily a result of solid state diffusion between the base materials. Figure 12 shows the phase formation diagram. Once the interfacial temperature falls below the eutectic temperature of 550 °C, the anomalous eutectic area is largely solidified. Subsequently, the solid state diffusion is initiated. Copper and zinc atoms diffuse toward the aluminum. Promoted by high thermal prerequisites, the IMLs are formed successively.

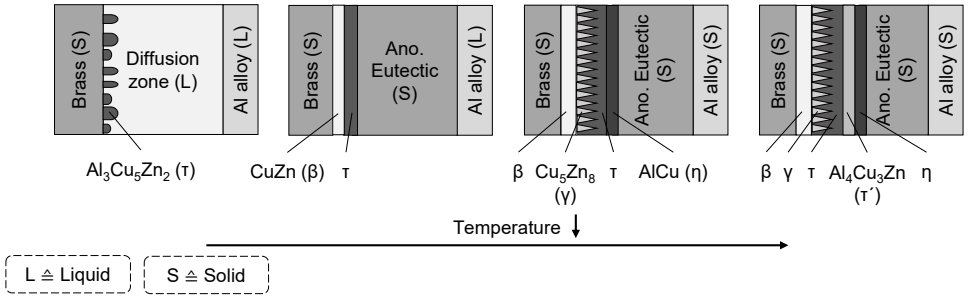

Figure 12: Diagram of phase formation process at the interface of brass and aluminum alloys

5.2. Continuous compound casting

Influence of casting speed

The influence of the average casting speed v_c on the interface formation was investigated experimentally and numerically. AA7075 is characterized by a susceptibility to hot tearing, which reduces the process flexibility. Therefore, the feasible casting speed setup is dominated by the shell material. The water volume flow rate per cooling circuit $\dot{V}_{water}$ was 1.2 l min^{-1} at a water inlet temperature $T_{water,in}$ of 60 °C. The AA7075 pouring temperature was 800 °C. The experiment design is presented in Table 3. It aims at the variation of the average casting speed v_c, while keeping the stroke length largely constant, if possible. The process window is limited by a minimum waiting time t_w, which was experimentally determined.

Average casting speed v_c [mm min^{-1}]	Stroke length [mm]	Waiting time t_w [s]
240	8	1.2
300	8	1.0
400	8	0.6
480	10	0.6
580	12	0.6

Table 3: Experiment design of casting speed variation

Figure 13 illustrates the stationary thermal profile within the graphite molds as a function of the average casting speed. Due to the premature tearing of the AA7075, an overall steady state was not achieved in the compound casting stage applying 580 mm min^{-1}. Nevertheless, it can be assumed

that the interfacial area exhibited quasi-stationary conditions. A casting speed increase leads to a spatial temperature level shift to higher values. This is a result of the raised enthalpy input into the casting system. The casting speed ascent causes an increase in the substrate temperature when entering the compound casting stage. The rim zone of the AA7075 layer most likely already solidifies in the cladding unit, especially in the case of low casting speeds. The increase in the casting speed rise was associated with the AA7075's susceptibility to hot tearing. Therefore, a waiting time of 0.6 s represents the lower possible limit within the present experimental setup. A sufficient process stability was achieved using casting speeds between 240 mm min^{-1} and 400 mm min^{-1}.

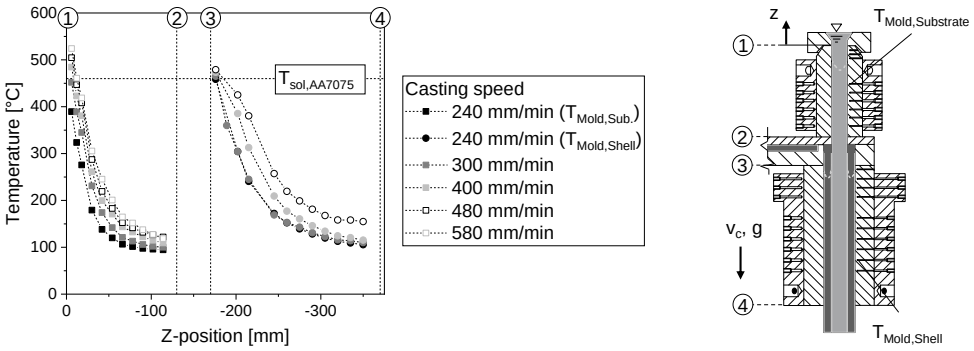

Figure 13: Thermal profile during continuous compound casting in dependence on the average casting speed

The calibrated simulation model supported the evaluation of the interfacial thermal conditions during compound casting. The process configurations are assessed against each other based on the characteristic substrate key figures *maximum interfacial temperature*, *maximum cooling rate after reaching*

the maximum thermal level, and *dwell time above* 550 °*C*. The casting speed increase has a significant influence on the maximum temperature level as well as on the cooling rate (see Figure 14). Thus, the result is a temperature ascent of about 10 % and a cooling rate increase of 60 %. The cooling rate increase is explained by the cooling effect of AA7075, as the substrate reaches the cladding unit with relatively high thermal prerequisites.

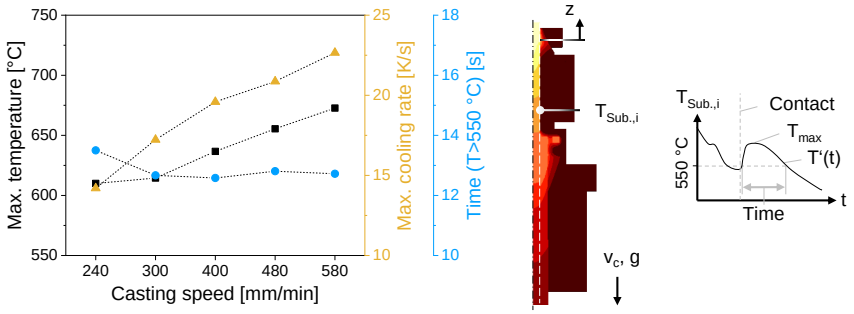

Figure 14: Calculated thermal conditions at the interface of bilayer rods in dependence on the average casting speed

Figure 15 shows unetched and etched micrographs of as-cast CuZn37/AA7075 samples. Raising the casting speed leads to an ascending metallurgical reaction between the joining partners. No metallurgical bonding was accomplished at an interfacial maximum temperature below 615 °C. When applying a casting speed of 300 mm min^{-1}, a partial cohesive bonding is apparent. The metallurgical bonding is enhanced by further increasing the casting speed. The influence of the casting speed is particularly evident in the formation of the anomalous eutectic layer. Its thickness is increased up to 400 µm. The high thermal conditions favor the dissolution process of copper and zinc in the shell layer. Furthermore, the casting speed increase is accompanied by a

strand acceleration ascent, which promotes fluid dynamic interactions at the interface and, consequently, intensifies the dissolution. The anomalous eutectic area exhibits a high degree of porosity, which is attributed to unfavorable feeding and contraction conditions of the dissolution area. The predominant grain growth direction of CuZn37 within a stroke is at an angle of 45 ° to the casting direction at the stroke beginning and 90 ° as the stroke progresses, and 100 ° at the stroke ending. The grain growth direction indicates the opposite heat transfer direction. The solidification of AA7075 is initiated at the inner surface of the graphite mold and also at the substrate surface. The two solidification fronts meet at the thermal center. It is a qualitative measure of the amount of heat dissipated into the casting tool and into the substrate. It enables a process evaluation at a macroscopic view and represents an important indicator to design a robust continuous compound casting process. It is determined through the identification of a rapid change in the AA7075 grain structure. The position of the thermal center varies in dependence on the average casting speed. The interface is characterized by cyclically appearing defects, which are attributed to the intermittent drawing kinematics. An unevenness of the substrate surface appears due to surface tension and gas entrapment when wetting between the cast materials occurs.

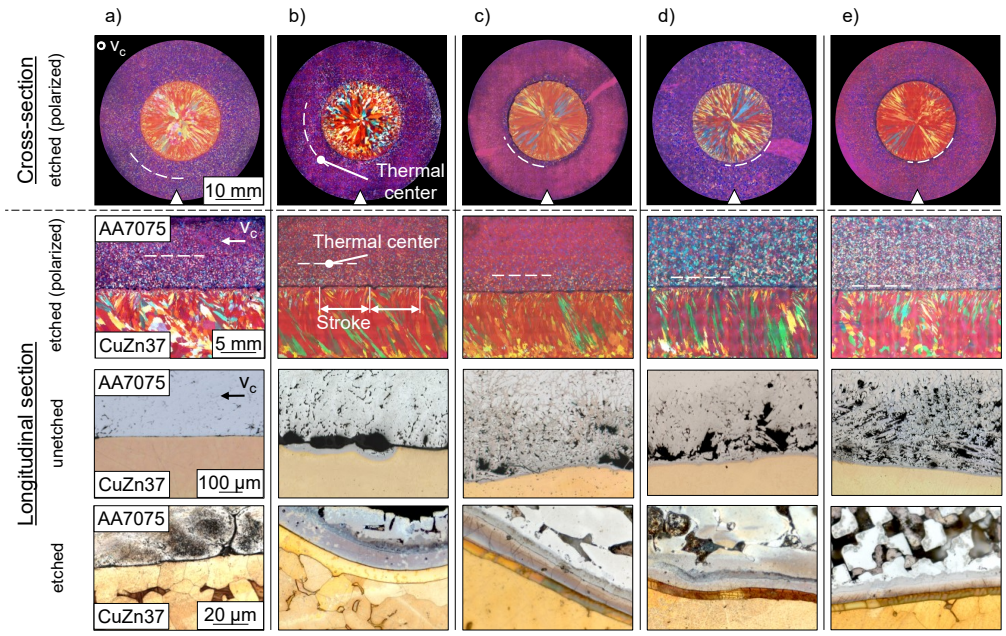

Figure 15: Macrostructure and microstructure of as-cast CuZn37/AA7075 samples in dependence on the casting speed: a) 240 mm min^{-1}, b) 300 mm min^{-1}, c) 400 mm min^{-1}, d) 480 mm min^{-1}, and e) 580 mm min^{-1}

The bonding strength of as-cast hybrid structures is analyzed by push-out testing. Figure 16 provides the testing results as a function of the average casting speed. The interdependence between bonding strength and casting speed has a degressive progression. The increase of about 10 N mm^{-2} is comparatively high between 240 mm min^{-1} and 400 mm min^{-1}, whereas a further casting speed increase does not significantly enhance the bonding strength. When applying a casting speed of 480 mm min^{-1} and 580 mm min^{-1}, the shear strength results exhibit a pronounced scattering. This effect can be explained by the stroke length increase. As the ratio of jointed and disjointed area within a stroke remains largely constant, the relatively small

thickness of push-out samples causes a high result scattering at high stroke lengths. Despite the absence of a metallurgical bonding at a casting speed of 240 mm min^{-1}, the samples provide a sufficient shear strength. The mechanical bonding between the joining partners is reinforced by microscopic interlocking due to the interfacial unevenness.

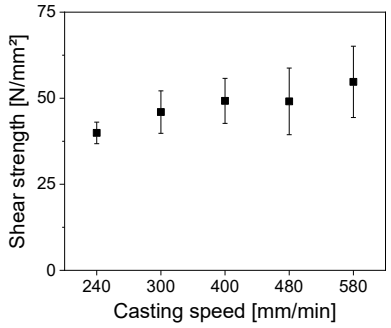

Figure 16: Shear strength of CuZn37/AA7075 samples in dependence on the casting speed

It is conclusive that a casting speed above 300 mm min^{-1} induces a pronounced cohesive bonding of the joint couple. However, the process stability suffers from a higher casting speed. 300 mm min^{-1} and 400 mm min^{-1} are promising compromises between metallurgical bonding and process stability. A mean bonding strength of 50 N mm^{-2} is achieved by applying a casting speed of 400 mm min^{-1}. A further increase in the casting speed does not significantly enhance the cohesive bonding.

Influence of cladding temperature

Assuming the other conditions to be similar, the influence of the thermal input of AA7075 on the interface formation was analyzed. The applied

average casting speed v_c was 300 mm min^{-1} (stroke length 8 mm, waiting time t_w 1.0 s). The AA7075 pouring temperature was varied between 800 °C and 900 °C. The heat dissipation into the melt basin and the cladding unit lowers the AA7075 temperature until the casting cavity is reached, so that the thermal level was at about 750 °C and 850 °C, respectively, when the first contact between substrate and shell occurred. The thermal profile of the graphite molds is shown in Figure 17. The temperature level of the substrate casting stage is largely independent of the cladding temperature, whereas the effect is clearly discernible from the compound casting stage. The cladding temperature increase shifts the isotherms in a negative z-direction. This is most apparent between a z-position of -200 mm and -250 mm.

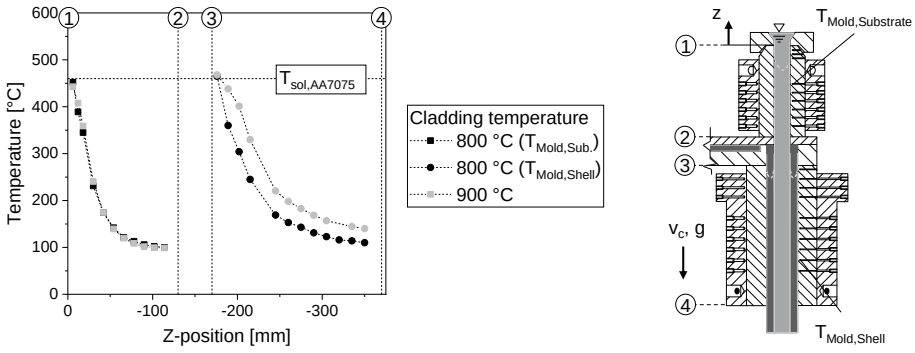

Figure 17: Thermal profile during continuous compound casting in dependence on the cladding temperature

The maximum level of the interfacial temperature raises from 614 °C to 678 °C (see Figure 18). Furthermore, the dwell time above 550 °C is longer. The maximum cooling rate is hardly affected by the change in the cladding temperature.

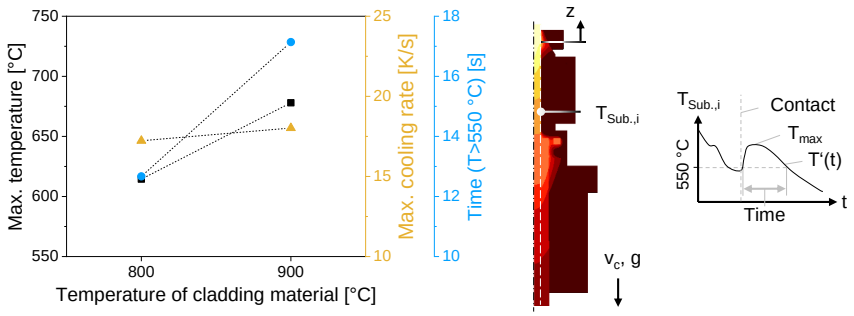

Figure 18: Calculated thermal conditions at the interface of bilayer rods in dependence on the cladding temperature

The etched and unetched micrographs of as-cast bilayer samples are shown in Figure 19. The poor metallurgical bonding of bilayer samples fabricated with a cladding temperature of 800 °C is enhanced by the elevation in the cladding temperature. However, a higher cladding temperature promotes the gas absorption in the aluminum melt and higher fluid dynamics. This causes a reduction of the geometrical concentricity of the layers and an elevation of the porosity in the anomalous eutectic area. The process stability is not negatively affected by the increase in the cladding temperature.

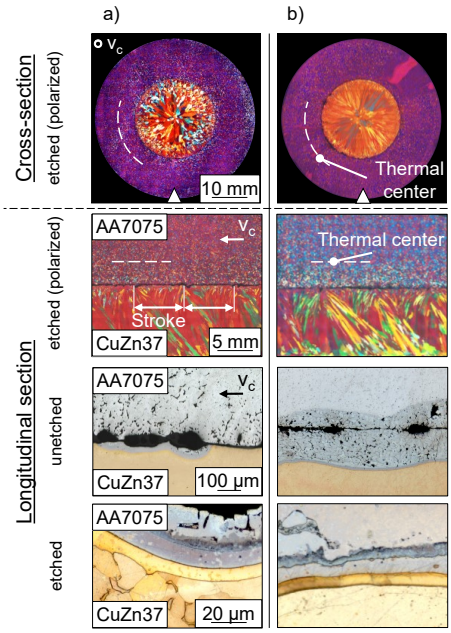

Figure 19: Macrostructure and microstructure of as-cast CuZn37/AA7075 samples in dependence on the cladding temperature: a) 800 °C and b) 900 °C

A higher cladding temperature partially compensates for the poor metallurgical bonding by applying a casting speed of 300 mm min^{-1} and a cladding temperature of 800 °C. As was shown by push-out testing, the bonding strength was enhanced by approximately 13 % (see Figure 20). Owing to the high degree of porosity, an elevated result scattering was apparent.

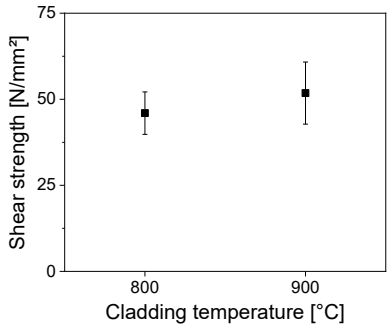

Figure 20: Shear strength of CuZn37/AA7075 samples in dependence on the cladding temperature

Influence of tool cooling conditions

The interdependence between tool tempering and interface formation was examined. The thermomanagement of the casting tool is predominantly controlled by the water inlet temperature $T_{water,in}$ and the water volume flow rate $\dot{V}_{water}$. The copper coolers of both stages provide two separate meander-shaped cooling channels in each component. The calculation of the heat dissipation through the cooling water $\dot{Q}_{water}$ is shown in Equation 1. The analytical calculation takes the simplification of temperature-independent thermophysical properties into account.

$$\dot{Q}_{water} = 2 \cdot \dot{V}_{water} \cdot \rho_{water} \cdot c_{p,water} \cdot (T_{water,out} - T_{water,in}) \qquad (1)$$

$c_{p,water} \triangleq$ Specific heat capacity of water [J kg^{-1}K^{-1}]
$\dot{Q}_{water} \triangleq$ Heat dissipation through water [W]
$T_{water,in} \triangleq$ Water inlet temperature [K]
$T_{water,out} \triangleq$ Water outlet temperature [K]
$\dot{V}_{water} \triangleq$ Water volume flow rate per cooling water channel [m^3 s^{-1}]
$\rho_{water} \triangleq$ Density of water [kg m^{-3}]

The experimental and numerical investigation plan is presented in Table 4. The average casting speed v_c was set to 400 mm min^{-1} (stroke length 8 mm, waiting time t_w 0.6 s) and the AA7075 pouring temperature to 800 °C.

Heat dissipation *sub. stage / compound casting stage* $\dot{Q}_{water}$ [kW]	Flow rate per channel *sub. stage / compound casting stage* $\dot{V}_{water}$ [l min^{-1}]	Water inlet temperature *sub. stage / compound casting stage* $T_{water,in}$ [°C]	Water outlet temperature *sub. stage / compound casting stage* $T_{water,out}$ [°C]
9.7/19.3	7.0/7.0	13/13	23/33
10.4/17.5	3.0/3.0	13/13	38/55
3.3/17.5*	1.2/3.0	60/13	80/55
5.3/17.5*	1.2/3.0	13/13	45/55
10.4/7.8*	3.0/1.2	13/13	38/60
3.3/4.9	1.2/1.2	60/60	80/90

Table 4: Experiment design of tool tempering variation

The thermal conditions of the graphite molds are plotted in Figure 21. The tool tempering significantly affects the temperature level. The temperature decreases from about 110 °C to 50 °C at a z-position of -114 mm and

*These particular investigations were only conducted numerically.

from 115 °C to 40 °C at -350 mm. The process stability is clearly increased by the elevation of the heat dissipation through the cooling water. A low water inlet temperature and high water volume flow rate favor a rapid solidification of AA7075. The rim zone of the shell is strengthened, which reduces the susceptibility to tearing.

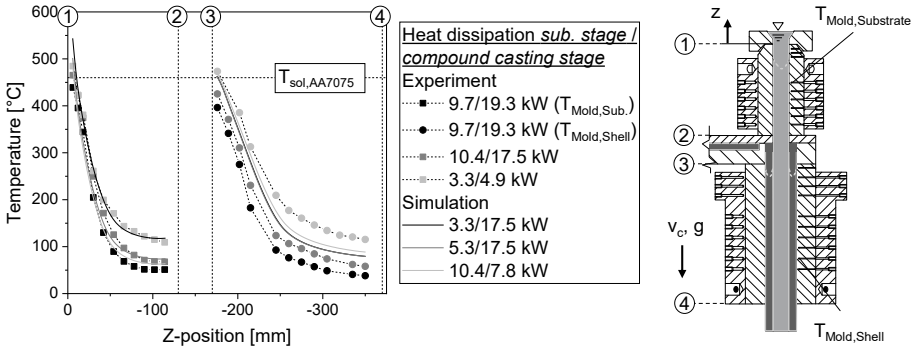

Figure 21: Thermal profile during continuous compound casting in dependence on the tool tempering

Figure 22 shows the numerically calculated interfacial temperature profile during compound casting. The influence of the heat dissipation through the cooling water is marginal. The increase in the maximum temperature level is about 1 %. The cooling rate reduction amounts to approximately 7 % and the dwell time decline to 7 %. The negligible interdependence between tool tempering conditions and thermal prerequisites at the interface is explained by three aspects. First, the wetting between the joining partners and the solidification of the AA7075 rim zone occurs predominantly in the cladding unit and in the upper area of the compound casting stage. The effect of the cooling water supply is relatively minor in these areas. Second, the heat

transfer between the bilayer rod and the casting tool is substantial when the cast alloy exhibits a liquid state and there is sufficient wetting between the components. As soon as the rim zone is formed and the strand lifts off, the cooling effect of the tool is substantially reduced. Lastly, the substrate layer is only indirectly cooled in the cladding and compound casting stage based on the format of the semi-finished product. As there is no direct contact between the tool and the substrate layer, the heat exchange occurs through the shell, which reduces the cooling effect.

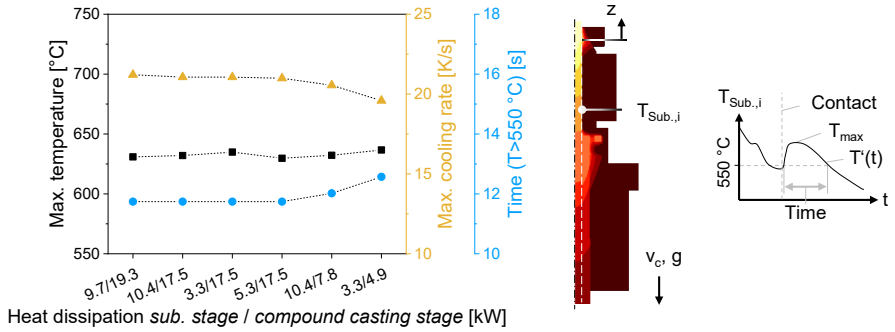

Figure 22: Calculated thermal conditions at the interface of bilayer rods in dependence on the tool tempering

The micrographs of as-cast bilayer samples are presented in Figure 23. The macrostructure of the bilayer samples are similar regardless of the disparate tool tempering conditions. A perceptible shift of the thermal center was not determined. The analysis of the microstructure yields a large-scale metallurgical bonding between the joining partners and a distinct anomalous eutectic area. Its layer thickness is slightly reduced through the elevation of the heat dissipation. However, this effect is negligible against the backdrop of

a high fluctuation of the anomalous eutectic layer thickness. The structural analysis sufficiently correlates with the procedural thermal key figures.

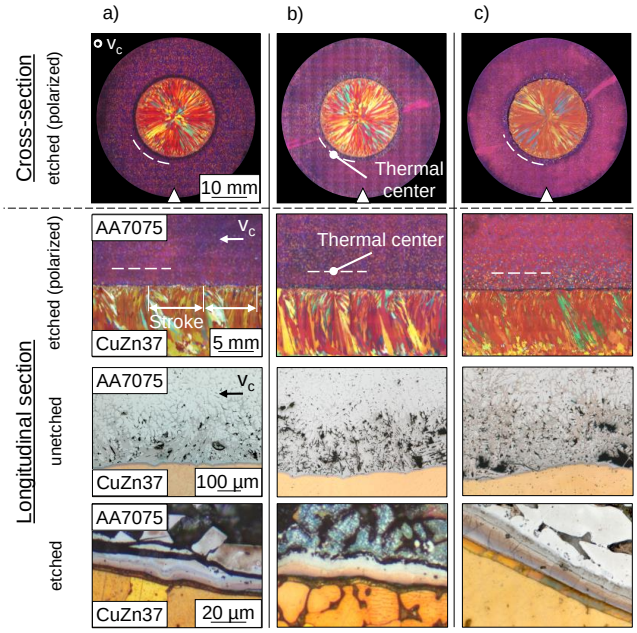

Figure 23: Macrostructure and microstructure of as-cast CuZn37/AA7075 samples in dependence on the heat dissipation through the cooling water: a) 9.7/19.3 kW, b) 10.4/17.5 kW, and c) 3.3/4.9 kW

The push-out testing results are shown in Figure 24. The shear strength is largely independent of the heat dissipation conditions. Thus, the mechanical characterization highly corresponds to the structural analysis. The reduction of the heat dissipation from 9.7/19.3 kW to 3.3/4.9 kW causes a slight increase of the bonding strength of approximately 6 %.

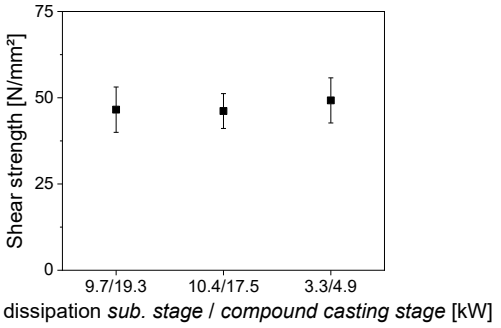

Figure 24: Shear strength of CuZn37/AA7075 samples in dependence on the tool tempering

6. Conclusion

A new strategy for single-step, continuous compound casting of copper/aluminum bilayer rods was developed and experimentally and numerically investigated. The procedure represents a highly industrially relevant production technique for the resource-efficient fabrication of load-adjusted, lightweight hybrid components. Fundamental findings on the metallurgical bonding of dissimilar joining partners and interdependencies between process parameters and interface formation were generated. The following conclusions can be drawn:

- The feasibility of metallurgical bonding using vertical continuous casting was demonstrated. The interfacial area was characterized by a large-scale anomalous eutectic area and four intermetallic layers. The two-phase character of the thickest IML was proven in this study. It is suspected that the particular phase is a blended phase composed of $Al_3Cu_5Zn_2$ and Cu_5Zn_8.

- A simulation model was built up in order to design the continuous compound casting process and evaluate the thermal interface conditions during compound casting. Applying an iterative calibration process, the experimentally determined temperature field was accurately modeled numerically.

- The average casting speed significantly influenced the process stability, as well as the interface formation. A casting speed of 300 mm min^{-1} and 400 mm min^{-1} represented a promising compromise. The average bonding strength in as-cast hybrid samples fabricated with a casting speed of 400 mm min^{-1} was about 50 N mm^{-2}.

- The ascent in the cladding temperature caused an increase in the enthalpy input. Consequently, a generally poor metallurgical bonding of the interface resulting from a low average casting speed could be compensated. However, undesired side effects occurred, such as excessive dissolution of copper and zinc in AA7075 and gas absorption and precipitation. The bonding between the joining partners was strengthened by the increase in the cladding temperature.

- The variation of the tool tempering conditions was of minor relevance with regard to the metallurgical bonding at the interface of bilayer rods. However, the process stability was significantly increased by elevating the water supply and reducing the water inlet temperature, as the rapid solidification of AA7075 favors the mechanical strength of the rim zone.

- The scientific investigations on the single-step, continuous compound casting of brass/aluminum bilayer components provide favorable prerequisites for a technology transfer to an industrial scale. The fundamental findings and scientific methods can be adapted to similar processes and formats of semi-finished products, such as pipes and strips. Additionally, the process concept is suitable for related material combinations, such as pure aluminum and pure copper. With regard to the fabrication of final products, the possibility to post-process as-cast hybrid structures has to be investigated. Relevant technologies here are extrusion, rolling, and forging.

7. Acknowledgment

This study was supported by the German Research Foundation (DFG) [grant number VO-1487/41-1]. The authors appreciate the financial funding from the DFG. Furthermore, the authors want to express their gratitude to Ms. Delphine Chassaing for her assistance in the sample preparation of the atom probe tomography. Lastly, the authors want to thank the scientific and technical staff of the Institute of Materials Science and Mechanics of Materials at the Technical University of Munich for their assistance with the EDS mapping and EBSD analysis.

8. References

Stets, W., 1998. Basics of materials science of compound casting of cast-iron alloys and steel material [Werkstoffkundliche Grundlagen des Verbundgießens von Gußeisenlegierungen mit Stahlwerkstoffen]. Dissertation, Ruhr University Bochum.

Nerl, C.J., 2014. Simulation-based process development for the continuous compound casting of aluminum semi-finished products [Simulationsgestützte Verfahrensentwicklung zum kontinuierlichen Verbundgießen von Aluminiumhalbzeugen]. Dissertation, Technical University of Munich.

Ißleib, A., Friedel, A., Lubojanski, I., 1995. Compound casting of iron-carbon alloys – fundamental metallurgical reactions at the interface – part II [Verbundgießen von Eisen-Kohlenstoff-Legierungen – grundlegende metallurgische Reaktionen an der Grenzfläche – Teil II]. Gießerei-Praxis 23/24, 442-447.

Papis, K.J.M., Hallstedt, B., Löffler, J.F., Uggowitzer, P.J., 2008. Interface formation in aluminium-aluminium compound casting. Acta Materialia 56, 3036-3043, http://doi.org/10.1016/j.actamat.2008.02.042.

Mittler, T., Greß, T., Feistle, M., Krinninger, M., Hofmann, U., Riedle, J., Golle, R., Volk, W., 2019. Fabrication and processing of metallurgically bonded copper bimetal sheets. Journal of Materials Processing Technology 263, 33-41, http://doi.org/10.1080/02670836.2018.1479946.

Pintore, M., Wölck, J., Mittler, T., Greß, T., Tonn, B., Volk, W., 2020. Composite casting and characterization of Cu-Al bilayer compounds. Inter-

national Journal of Metalcasting 14, 155-166, http://doi.org/10.1007/s40962-019-00344-x.

Jiang, W., Fan, Z., Li, C., 2015. Improved steel/aluminum bonding in bimetallic castings by a compound casting process. Journal of Materials Processing Technology 226, 25-31, https://doi.org/10.1016/j.jmatprotec.2015.06.032.

Jiang, Z., Fan, Z., Wenming, J., Li, G., Wu, Y., Guan, F., Jiang, H., 2018. Interfacial microstructures and mechanical properties of Mg/Al bimetal produced by a novel liquid-liquid compound casting process. Journal of Materials Processing Technology 261, 149-158, https://doi.org/10.1016/j.jmatprotec.2018.06.013.

Dong, L., Chen, W., Huo, L., Liu, Y., Luo, Q., 2016. Metallurgical process analysis and microstructure characterization of the bonding interface of QAl9-4 aluminum bronze and 304 stainless steel composite materials. Journal of Materials Processing Technology 238, 325-332, https://doi.org/10.1016/j.jmatprotec.2016.07.041.

Zare, G.R., Divandari, M., Arabi, H., 2013. Investigation on interface of Al/Cu couples in compound casting. Materials Science and Technology 29, 190-196, https://doi.org/10.1179/1743284712Y.0000000096.

Pintore, M., Starykov, O, Mittler, T., Volk, W., Tonn, B., 2018. Experimental investigations on the influence of the thermal conditions during composite casting on the microstructure of Cu-Al bilayer compounds. International Journal of Metalcasting 12, 79-88, https://doi.org/10.1007/s40962-017-0140-0.

Luo, J.-T., Zhao, S.-J., Zhang, C.-X., 2011. Microstructure of aluminum/ copper clad composite fabricated by casting-cold extrusion forming. Journal of Central South University of Technology 18, 1013-1017, https://doi.org/10.1007/s11771-011-0796-1.

Luo, J.-T., Zhao, S.-J., Zhang, C.-X., 2012. Casting–cold extrusion of Al/Cu clad composites by copper tubes with different sketch sections. Journal of Central South University of Technology 19, 882-886, https://doi.org/10.1007/s11771-012-1087-1.

Jiang, W., Li, G., Fan, Z., Wang, L., Liu, F., 2016. Investigation on the interface characteristics of Al/Mg bimetallic castings by lost foam casting. Metallurgical and Materials Transactions A 47, 24622-2470, https://doi.org/10.1007/s11661-016-3395-9.

Fu, Y., Zhang, Y.-B., Jie, J.-C., Svynarenko, K., Liang, C.-H., Li, T.-J., 2017. Interfacial phase formation of Al-Cu bimetal by solid-liquid casting method. China Foundry 14, 194-198, https://doi.org/10.1007/s41230-017-6057-7.

Jiang, W., Guan, F., Li, G., Jiang, H., Zhu, J., Fan, Z., 2019. Processing of Al/Cu bimetal via a novel compound casting method. Materials and Manufacturing Processes 34, 1016-1025, https://doi.org/10.1080/10426914.2019.1615084.

Akbarifar, M., Divandari, M., 2017. On the interfacial characteristics of compound cast Al/brass bimetals. International Journal of Metalcasting 11, 506-512, https://doi.org/10.1007/s40962-016-0101-z.

Gholami, M., Divandari, M., 2017. Interfacial phases and defects characteristics of Al/Cu-Zn bimetal produced via centrifugal casting process. Iranian Journal of Materials Science and Engineering 15, 52-61, https://doi.org/10.22068/ijmse.15.4.52.

Haga, T., Nakamura, R., Kumai, S., Watari, H., 2009. Clad strip casting by a twin roll caster. Archives of Materials Science and Engineering 37, 117-124.

Xing, H, Haitao, Z., Bo, S., Kesheng, Z., Lizi, H., Ke, Q., Jianzhong, C., 2015. Numerical simulation and preparation of cladding billet by direct chill semi-continuous casting. Materials Transactions 56, 1893-1900, https://doi.org/10.2320/matertrans.M2015229.

Zhang, W., Gao, J., Rohatgi, K., Zhao, H., Li, Y., 2009. Effect of the depth of the submerged entry nozzle in the mold on heat, flow and solution transport in double-stream-pouring continuous casting. Journal of Materials Processing Technology 209, 5536-5544, https://doi.org/10.1016/j.jmatprotec.2009.05.009.

Yan, G.-Y., Mao, F., Wu, W., Cao, Z.-Q., Wang, T.-M., Li, T.-J., 2016. Characteristics evolution of 6009/7050 bimetal slab prepared by direct-chill casting process. Transaction of Nonferrous Metals Society of China 26, 895-904, https://doi.org/10.1016/S1003-6326(16)64184-5.

Li, Y.-Y., Zheng, X.-P., Zhang, W.-W., Luo, Z.-Q., 2009. Effect of deformation temperature on microstructures and properties of 7075/6009 alloy. Transaction of Nonferrous Metals Society of China 19, 1037-1043,

https://doi.org/10.1016/S1003-6326(08)60403-3.

Anderson, M.D., Kubo, K.T., Bischoff, T.F., Fenton, W.J., Reeves, E.W., Spendlove, B., Wagstaff, R.B., 2005. Method for casting composite ingot. Patent US 2005/0011630 A1.

Nerl, C., Wimmer, M., Hoffmann, H., Kaschnitz, E., Langbein, F., Volk, W., 2014. Development of a continuous composite casting process for the production of bilayer aluminium strips. Journal of Materials Processing Technology 214, 1445-1455, http://doi.org/10.1016/j.jmatprotec.2014.02.018.

Heugenhauser, S., Kaschnitz, E., Schumacher, P., 2020. Development of an aluminum compound casting process – experiments and numerical simulations. Journal of Materials Processing Technology 279, https://doi.org/10.1016/j.jmatprotec.2019.116578.

Greß, T., Mittler, T., Volk, W., 2020. Casting methods for the production of rotationally symmetric copper bimetals. Materials Science and Technology 36, 906-916, https://doi.org/10.1080/02670836.2018.1479946.

Xie, J., Wu, C., Liu, X., Liu, X., 2007. A novel forming process of copper cladding aluminum composite materials with core-filling continuous casting. Materials Science Forum 539-543, 956-961, https://doi.org/10.4028/www.scientific.net/MSF.539-543.956.

Su, Y.-J., Liu, X.-H., Huang, H.-Y., Wu, C.-J. Liu, X.-F., Xie, J.-X., 2011. Effects of processing parameters on the fabrication of copper cladding aluminum rods by horizontal core-filling continuous casting. Metallurgical and Materials Transactions B 42, 104-113, https://doi.org/10.1007/s11663-

010-9449-2.

Greß, T., Glück Nardi, V., Mittler, T., Schmid, S., Buchberger, P., Tonn, B., Volk, W., 2020. Interface formation and characterization of brass/aluminum compounds fabricated through die casting and semi-continuous casting. International Journal of Metalcasting 14, 564-579, https://doi.org/10.1007/s40962-019-00387-0.

Gnielinski, V., 1976. New equations for heat and mass transfer in turbulent pipe and channel flow. International Chemical Engineering, 359-368.

Klose, C., Freytag, P., Otten, M., Thürer, S.E., Maier, H.J., 2018. Thermal properties of intermetallic phases at the interface of aluminum-copper compound castings. Advanced Engineering Materials 20, 1-10, https://doi.org/10.1002/adem.201701027.

Greß, T., Mittler, T., Schmid, S., Chen, H., Ben Khalifa, N., Volk, W., 2019. Thermal analysis and production of as-cast Al 7075/6060 bilayer billets. International Journal of Metalcasting 13, 817-829, https://doi.org/10.1007/s40962-018-0282-8.

Greß, T., Stahl, J., Mittler, T., Spano, L., Chen, H., Ben Khalifa, N., Volk, W., 2019. Mechanical characterization of as-cast AA7075/6060 and CuSn6/Cu99.5 compounds using an experimental and numerical push-out test. Materials Science & Engineering: A 751, 214-225, https://doi.org/10.1016/j.msea.2019.02.080.

Greß, T., Gruber, M., Stahl, J., Wittmann, S., Steinlehner, F., Glück Nardi, V., Tonn, B., Volk, W., 2020. Experimental and numerical investiga-

tions into the deformation and fracture behavior of intermetallics and base materials in as-cast Al-Cu compounds. Materials Today Communications 25, https://doi.org/10.1016/j.mtcomm.2020.101278.

Moody, M.P., Stephenson, L.T., Ceguerra, A.V., Ringer, S.P., 2008. Quantitative binomial distribution analyses of nanoscale like-solute atom clustering and segregation in atom probe tomography data. Microscopy Research & Technique 71, 542-550, https://doi.org/10.1002/jemt.20582.

Bogno, A.-A., Valloton, J., Jimenez, D.D., Rappaz, M., Henein, H., 2019. Rapid solidification of Al-Cu droplets of near eutectic composition. Materials Science and Engineering 529, 1-6.

Mueller, B.A., Perepezko, J.H., 1988. Microstructure development in undercooled Al-Al_2Cu alloys. Materials Science and Engineering 98, 153-156, https://doi.org/10.1016/0025-5416(88)90145-0.

Prasad, A., Henein, H., Maire, E., Gandin, C.A., 2004. X-ray tomography study of atomized Al-Cu droplets. Canadian Metallurgical Quarterly 43, 273-282, https://doi.org/10.1179/cmq.2004.43.2.273.

Degtyareva, V.F., Degtyareva, O., Sakharov, M.K., Novokhatskaya, N.I., Dera, P., Mao, H.K., Hemley, R.J., 2005. Stability of Hume-Rothery phases in CuZn alloys at pressures up to 50 GPa. Journal of Physics: Condensed Matter 17, 7955-7962, https://doi.org/10.1088/0953-8984/17/50/013.

Eckerlin, P., Kandler, H., 1971. Structure Data of Elements and Intermetallic Phases. In: Condensed Matter. Ed. by K.-H. Hellwege, A.M. Hellwege. Berlin Heidelberg: Springer.

Divandari, M., Vahid Golpayegani, A.R., 2009. Study of Al/Cu rich phases formed in A356 alloy by inserting Cu wire in pattern in LFC process. Materials and Design 30, 3279-3285, https://doi.org/10.1016/j.matdes.2009.01.008.

List of Figures

List of Tables